



Cite this: *RSC Adv.*, 2017, 7, 37929

Core@shell $\text{Fe}_3\text{O}_4@\text{Mn}^{2+}$ -doped $\text{NaYF}_4:\text{Yb}/\text{Tm}$ nanoparticles for triple-modality T_1/T_2 -weighted MRI and NIR-to-NIR upconversion luminescence imaging agents

Yang Luo, Sinan Du, Wei Zhang, Zhengfang Liao, Fang Zuo ^{*} and Shengtao Yang ^{*}

Core@shell structures of $\text{Fe}_3\text{O}_4@\text{Mn}^{2+}$ -doped $\text{NaYF}_4:\text{Yb}/\text{Tm}$ nanoparticles (NPs) with multifunctional properties were prepared using a hydrothermal route with a seed-growth procedure. The effect of Mn^{2+} ions on the phase, shape, and upconversion luminescence (UCL) of $\text{Fe}_3\text{O}_4@\text{Mn}^{2+}$ -doped $\text{NaYF}_4:\text{Yb}/\text{Tm}$ NPs was explored using X-ray diffraction, transmission electron microscopy, dynamic light scattering, and photoluminescence spectroscopy. Furthermore, hydrophobic to hydrophilic surface modification of the $\text{Fe}_3\text{O}_4@\text{Mn}^{2+}$ -doped $\text{NaYF}_4:\text{Yb}/\text{Tm}$ NPs was achieved by coating the NPs with an amphiphilic polymer (poly(maleic anhydride-*alt*-1-octadecene) (C_{18}PMH)) modified with amine-functionalized methyl ether poly(ethylene glycol). Then, the NIR-to-NIR UCL ascribed to the Tm^{3+} ions, T_1 -weighted MRI ascribed to the Mn^{2+} ions, and T_2 -weighted MRI ascribed to the Fe_3O_4 core of the hydrophilic $\text{Fe}_3\text{O}_4@\text{Mn}^{2+}$ -doped $\text{NaYF}_4:\text{Yb}/\text{Tm}$ NPs were evaluated. The results indicate that Mn^{2+} doping is an effective method to control the size/shape and improve the UCL intensity of $\text{Fe}_3\text{O}_4@\text{Mn}^{2+}$ -doped $\text{NaYF}_4:\text{Yb}/\text{Tm}$ NPs, which are promising as imaging agents for NIR-to-NIR UCL and T_1/T_2 -weighted MRI in biomedical research.

Received 6th July 2017
Accepted 26th July 2017

DOI: 10.1039/c7ra07460c

rsc.li/rsc-advances

1. Introduction

Multimodal imaging using functional nanoparticles (NPs) is receiving considerable attention because it can combine the advantages of different imaging modes and improve the efficiency of diagnosis and research.^{1–3} Bifunctional magnetic and luminescent nanomaterials have received considerable attention for multimodal imaging because they provide high sensitivity/resolution fluorescence imaging, and non-invasive and high spatial resolution magnetic resonance imaging (MRI) for real-time monitoring.^{4–7}

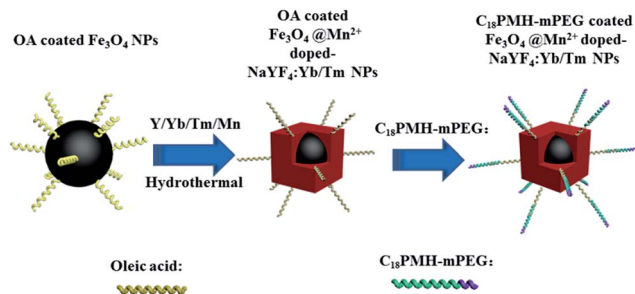
Among the various luminescent materials, lanthanide-doped upconversion nanoparticles (UCNPs), which can convert long wavelength near-infrared (NIR) radiation into a visible or NIR emission through an upconversion process, have received a growing amount of interest. Lanthanide-doped UCNPs exhibit higher signal-to-noise ratios, deeper tissue penetration, and lower photodamage than conventional luminescent probes, rendering them ideal for use as luminescent probes in bioimaging.^{8–14} UCNPs based on NIR-to-NIR emission are more suitable for upconversion optical bioimaging because the biological transparent window is located at 700–1000 nm.^{3,15–17} Tm-Doped UCNPs have attracted particular interest because they can emit NIR light

at approximately 800 nm under 980 nm excitation.^{3,15–17} However, the application of UCNPs is still restricted because of their low upconversion luminescence (UCL) efficiency. Until now, co-doping with non-lanthanide ions to tailor the local crystal field of the lanthanide ions has been regarded as an effective strategy to improve the UCL efficiency.^{17–19} Mn^{2+} ions have been regarded as promising doping ions for UCNPs because they provide a simultaneous enhancement of the upconversion emission and control of the crystal phase/size.^{20–27}

Based on the different roles that they play in imaging, MRI contrast agents can be divided into two categories: T_1 -weighted contrast agents and T_2 -weighted contrast agents.^{28–30} T_1 -weighted MRI contrast agents make the tissue brighter than the surrounding environment,^{28,31,32} whereas T_2 -weighted MRI contrast agents make the contrast parts darker.^{28,33,34} Traditional MRI using T_1 - or T_2 -weighted contrast agents has certain limitations related to the refinement of signals that originate from artifacts (such as fat, calcification, hemorrhages, air) other than diseased lesions.^{29,35} These agents complicate the image and, in most cases, make it difficult to map the area of disease spread. One of the solutions for this problem is to design a T_1/T_2 weighted dual mode contrast agent that can provide more detailed pathological information for the diagnosis and monitoring of cancer treatment.^{28–30} Usually, paramagnetic compounds, such as Mn-based coordination complexes and NPs, can be used as T_1 -weighted contrast agents.^{36,37} Gu and co-workers confirmed that

College of Chemistry & Environment Protection Engineering, Southwest Minzu University, Chengdu 610041, China. E-mail: polymerzf@swun.cn; yangst@pku.edu.cn





Scheme 1 Schematic representation of the formation of $\text{Fe}_3\text{O}_4@\text{Mn}^{2+}$ -doped $\text{NaYF}_4:\text{Yb/Tm}$ NPs and their subsequent transfer to water.

Mn^{2+} -doped $\text{NaYF}_4:\text{Yb/Er}$ UCNPs can be used as T_1 mode contrast agents.²¹ Generally speaking, T_2 -weighted MRI contrast agents are based on superparamagnetic nanomaterials (e.g., Fe_3O_4), which have large magnetization values.^{38,39} Consequently, the combination of Fe_3O_4 with the Mn^{2+} -doped $\text{NaYF}_4:\text{Yb/Tm}$ system can provide a simple strategy to construct the NIR-to-NIR UCL and a binary T_1/T_2 -weighted triple-modality imaging probe.

In the precious work, we applied a seed-growth procedure to synthesize hydrophobic $\text{Fe}_3\text{O}_4@\text{Mn}^{2+}$ -doped $\text{NaYF}_4:\text{Yb/Er}$ core@shell-structured NPs using oleic acid (OA)-coated Fe_3O_4 NPs as the seeds and core, these NPs can emit red UCL.⁸ In that work, we proved that these core@shell-structured NPs can be obtained by hydrothermal method.⁸ However, the luminescence intensity of these $\text{Fe}_3\text{O}_4@\text{Mn}^{2+}$ -doped $\text{NaYF}_4:\text{Yb/Er}$ NPs in water was significantly reduced compared to the original hydrophobic NPs when using a ligand exchange method, the quenching effect is mainly caused by the nonradiative decay of the electronically excited states of the dopant lanthanide ions caused by surface ligands and water molecules.^{8,40,41} It was found that compared with the ligand exchange method, the amphiphilic polymer coating method can maintain better UCL intensity ascribed to the presence of hydrophobic OA ligands in the later case, which could hinder at least partly the direct access of water molecules to the particle surface.^{40,41} Herein, we applied our reported method to synthesize new hydrophobic $\text{Fe}_3\text{O}_4@\text{Mn}^{2+}$ -doped $\text{NaYF}_4:\text{Yb/Tm}$ core@shell-structured NPs. The overall synthetic procedure is illustrated in Scheme 1. The crystal phase and morphology of these UCNPs were tuned by doping Mn^{2+} . Then, the hydrophobic $\text{Fe}_3\text{O}_4@\text{Mn}^{2+}$ -doped $\text{NaYF}_4:\text{Yb/Tm}$ NPs could be transferred into water after coating them with a layer of amphiphilic poly(maleic anhydride-*alt*-1-octadecene) (C_{18}PMH) modified with amine-functionalized methyl ether poly(ethylene glycol) ($\text{C}_{18}\text{PMH-mPEG}$). Finally, the obtained hydrophilic UCNPs were used as contrast agents for NIR-to-NIR luminescent imaging and T_1/T_2 -weighted MRI.

2. Experimental

2.1. Materials

All chemicals were of analytical grade and used as received without further purification. Deionized water was used throughout. Yttrium nitrate hexahydrate (99.99% trace metals

basis), ytterbium nitrate (99.99% trace metals basis), and thulium(III) nitrate hexahydrate (99.9% trace metals basis) were supplied by Best Chemical Reagent Co., Ltd. (Chengdu, China). OA (technical grade, 98.0%), sodium fluoride (reagent grade, 98.0%), sodium hydroxide (reagent grade, 96%), ethanol (reagent grade, 99.7%), ferric trichloride hexahydrate (reagent grade, 99.0%), and manganese dichloride tetrahydrate (reagent grade, 98.0%) were supplied by Kelong Chemical Technology Co., Ltd. (Chengdu, China). Toluene (reagent grade, 99.5%), chloroform (reagent grade, 99.0%), and dichloromethane (reagent grade, 99.0%) were purchased from Ruijinte Chemical Technology Co., Ltd. (Tianjin, China). Ferrous sulfate heptahydrate (reagent grade, 99%) was supplied by Jinshan Chemical Technology Co., Ltd. (Chengdu, China). Ammonia solution (reagent grade, 28%) and triethylamine (TEA) were supplied by Kelong Chemical Technology Co., Ltd. (Chengdu, China). C_{18}PMH was supplied by Sigma-Aldrich Co., LLC. (USA). Methoxypolyethylene glycol amine (mPEG-NH₂) was supplied by Aladdin Company (Shanghai, China). 1-Ethyl-3-(3-(dimethylamino)propyl) carbodiimide hydrochloride (EDC·HCl) was obtained from Best Chemical Reagent Co., Ltd. (Chengdu, China).

2.2. Synthesis of $\text{C}_{18}\text{PMH-mPEG}$

In a typical procedure,^{42,43} poly(maleic anhydride-*alt*-1-octadecene) (10 mg, 0.0286 mmol, C_{18}PMH) was reacted with methoxypolyethylene glycol amine (142.85 mg, 0.0286 mmol, mPEG-NH₂ 5 kDa) in 10 mL of $\text{CH}_2\text{Cl}_2/\text{TEA}$ (9 : 1, v/v) for 2 h at room temperature. Then, EDC·HCl (10.9 mg, 0.055 mmol) was added, and the solution was stirring for another 24 h. The resulting polymer was dialyzed against ultrapure water through a dialysis membrane (molecular weight cut-off of 8000–14 000) for 2 days. Finally, the $\text{C}_{18}\text{PMH-mPEG}$ powders were obtained by lyophilization. ¹H NMR (400 MHz, CDCl_3) δ : 3.7–3.4 (m, br, CH_2 of mPEG), 1.3–1.0 (m, CH_2 of C_{18}PMH), 1.65 ppm (s, br, CH of C_{18}PMH), 0.88 ppm (m, br, CH_3 of C_{18}PMH).

2.3. Synthesis of OA coated $\text{Fe}_3\text{O}_4@\text{Mn}^{2+}$ -doped $\text{NaYF}_4:\text{Yb/Tm}$ NPs

First, the hydrophobic OA-coated Fe_3O_4 NPs were prepared according to our previously reported procedure⁴⁴ and then dispersed in toluene for use in the next step. The as-prepared OA- Fe_3O_4 NPs were used as seeds and covered with an NIR shell using a facile hydrothermal method, which was similar to the preparation of Mn^{2+} -doped $\text{NaYF}_4:\text{Yb/Er}$ NPs.⁸ $\text{Fe}_3\text{O}_4@\text{NaYF}_4:18\% \text{Yb}/2\% \text{Tm}/x \text{Mn}$ ($x = 0, 20, 30, 40$, and 50 mol%) UCNPs were prepared using a hydrothermal method with OA as a capping ligand. In a typical procedure, $\text{Fe}_3\text{O}_4@\text{NaYF}_4:18\% \text{Yb}/2\% \text{Tm}/40\% \text{Mn}$ NPs (as an example), 3.135 mL of 0.5 M MnCl_2 , 3.135 mL of 0.5 M $\text{Y}(\text{NO}_3)_3$, 3.53 mL of 0.2 M $\text{Yb}(\text{NO}_3)_3$, and 0.41 mL of a 0.2 M $\text{Tm}(\text{NO}_3)_3$ aqueous solution were added to a mixture of NaOH (1.164 g), 5.88 mL toluene dispersion of OA coated Fe_3O_4 (5 mg mL^{-1}), OA (19.58 mL), and ethanol (39.16 mL) under stirring. Then, 7.83 mL of deionized water containing 18.5 mmol NaF was added dropwise into the mixture. After vigorous stirring at room temperature for 30 min, the colloidal



solution was transferred into a 100 mL Teflon-lined autoclave, which was sealed and heated at 200 °C for 8 h; then, the mixture was cooled to room temperature. The final product was collected using magnetic separation and then washed several times with ethanol and deionized water. Finally, the obtained OA-Fe₃O₄@NaYF₄:18% Yb/2% Tm/40% Mn NPs were dispersed in chloroform.

2.4. Synthesis of C₁₈PMH-mPEG coated Fe₃O₄@40% Mn²⁺-doped NaYF₄:Yb/Tm NPs

The synthesis of mPEG-Fe₃O₄@NaYF₄:18% Yb/2% Tm/40% Mn NPs was performed according to a previously reported method.⁴³ C₁₈PMH-mPEG (15 mg) and OA coated Fe₃O₄@40% Mn²⁺-doped NaYF₄:Yb/Tm NPs (15 mg) were dispersed separately in chloroform (10 mL) and then mixed together to obtain a homogeneous phase. The mixture was stirred for 2 h at room temperature. After evaporating the chloroform, the black solid was redispersed in 10 mL of water, and the large aggregates were removed using a 0.22 μm drainage membrane filter and stored at 4 °C.

2.5. Cytotoxicity assay

The cell viability was measured using a 3-(4,5 dimethylthiazol-2-yl)-2,5-diphenyltetrazolium bromide (MTT) proliferation assay.^{45,46} Briefly, HeLa cells were seeded into 96-well plates with 200 μL of fresh medium at a density of 1 × 10⁴ cells per well and cultured at 37 °C and 5% CO₂ overnight. The cell culture medium in each well was then replaced by 200 μL of cell growth medium containing C₁₈PMH-mPEG coated Fe₃O₄@40% Mn²⁺-doped NaYF₄:Yb/Tm NPs at concentrations ranging from 0.0625 to 1 mg mL⁻¹. After incubation for 24 h, 200 μL of MTT (0.5 mg mL⁻¹ in a phosphate-buffered saline solution) was added to each well for a further 4 h incubation at 37 °C. The growth medium was removed gently using suction, 300 μL of dimethyl sulfoxide was added to each well as a solubilizing agent, and the microplate was left at room temperature for 2 h.

2.6. In vivo UCL imaging

Firstly, 100 μL of C₁₈PMH-mPEG coated Fe₃O₄@40% Mn²⁺-doped NaYF₄:Yb/Tm NPs (0.8 mg mL⁻¹) was injected intradermally into the subcutaneous tissue of nude mice. In this system, two external adjustable CW 980 nm lasers (0–5 W) (Shanghai Connet Fiber Optics Co., China) were used as the excitation source, and an Andor DU897 EMCCD was used as the signal collector. Images of luminescent signals were analyzed using the Kodak Molecular Imaging software.

2.7. In vitro T₁/T₂-weighted MRI

Initially, 2 mL of the C₁₈PMH-mPEG coated Fe₃O₄@40% Mn²⁺-doped NaYF₄:Yb/Tm NPs solution at Mn concentrations of 0, 0.0346, 0.0691, 0.1382, 0.2763, and 0.5526 mM or Fe concentrations of 0, 0.0973, 0.2434, 0.4868, 0.9737, and 1.9474 mM were prepared before MRI. Both T₁-weighted and T₂-weighted magnetic resonance (MR) images were acquired using a 0.5 T MesoMR23-060H NMR analyzing and imaging system (Shanghai Niumag

Corporation, Shanghai, China). The parameters were set as follows: Q-IR sequence, field of view (FOV) read = 100 mm, FOV phase = 100 mm, TR = 300 ms, TE = 9.5 ms, slices = 1, slice width = 5 mm, averages = 10, *k*-space size = 192 × 256 for T₁-weighted MRI, and Q-CPMG sequence, FOV read = 100 mm, FOV phase = 100 mm, TR = 3000 ms, TE = 80 ms, slices = 1, slice width = 5 mm, averages = 10, *k*-space size = 192 × 256 for T₂-weighted MRI. The relaxivities (*r*₁ and *r*₂) were calculated from a linear fitting of the inverse relaxation time as a function of the Fe or Mn²⁺ concentration.

2.8. Characterization

The morphology, microstructure, and magnetic properties of the as-prepared NPs were characterized using transmission electron microscopy (TEM; Tecnai F20). The structure was studied using X-ray diffraction (XRD) measurements (Rigaku D/max-2500 V/PC) with Cu Kα radiation (*λ* = 0.154 nm). The magnetic properties were assessed using a vibrating sample magnetometer (HH-15, China) at 25 °C under an applied magnetic field. The UCL spectra were recorded using a Hitachi F-4600 fluorescent spectrometer with a 980 nm diode laser. Fourier transform infrared (FTIR) spectra were recorded using a Spectrum One instrument (PerkinElmer) and a KBr pellet in the spectral range of 4000 to 500 cm⁻¹. The ¹H NMR spectra of methoxy poly(ethylene glycol) phosphoric acid were recorded on an Agilent Technologies 400/54 Annual Refill (400 MR) NMR instrument using CDCl₃ as a solvent with a small amount of tetramethylsilane as an internal standard. An inductively coupled plasma mass spectrometry (ICP-MS) system (Shimadzu Corp., Japan) was used to analyze the element concentration of the solution. The T₁/T₂ relaxation times of the particle suspensions with different Fe concentrations (0.0973–1.9474 mM) or Mn²⁺ concentrations (0.0346–0.5526 mM) in water were measured using a 0.5 T MesoMR23-060H NMR analyzing and imaging system (Shanghai Niumag Corporation, Shanghai, China).

3. Results and discussion

3.1. Effect of Mn²⁺ ion doping on the morphology, nanostructure, and UCL of Fe₃O₄@Mn²⁺-doped NaYF₄:Yb/Tm NPs

Fe₃O₄@Mn²⁺-doped NaYF₄:Yb/Tm NPs were synthesized by the nucleation and growth of Mn²⁺-doped NaYF₄:Yb/Tm on pre-formed Fe₃O₄ NPs. Previous studies showed that the doping of Mn²⁺ ions could tune the crystal structure, shape/size, and UCL of the UCNPs.^{20–27} Five samples were synthesized, each doped with 18 mol% Yb³⁺, 2 mol.

% Tm³⁺, and 0–50 mol% Mn²⁺ ions, to investigate the effect of Mn²⁺ doping on the preparation of Fe₃O₄@Mn²⁺-doped NaYF₄:Yb/Tm NPs. Then, the crystal structure and phase purity of the five samples were examined using XRD, as shown in Fig. 1. Mn-free UCNPs exhibit both cubic (Joint Committee on Powder Diffraction Standards (JCPDS file number 77-2042) and hexagonal (JCPDS file number 16-0334)) structures (Fig. 1a). Furthermore, the phase transformation from the coexistence of



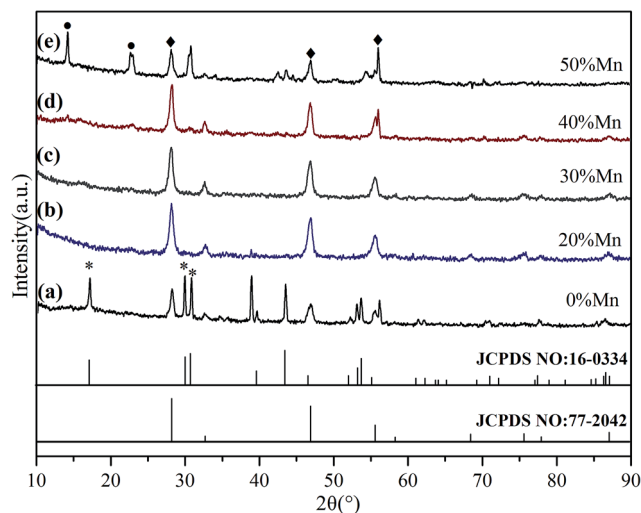


Fig. 1 XRD patterns of OA coated $\text{Fe}_3\text{O}_4@ \text{NaYF}_4:\text{Yb/Tm}$ NPs co-doped with 0, 20, 30, 40, and 50 mol% Mn^{2+} . The diffraction peaks of the cubic phase are marked with ◆, and peaks related to the hexagonal phase are marked with *. The black dots in curve e indicate a possible extra phase of $\text{NaMn}_3\text{F}_{10}$.

α - and β -phases to the pure α -phase is completed by increasing the Mn^{2+} content; the pure α -phase can be obtained when the Mn^{2+} content reaches 20 mol% (Fig. 1b), and no other diffraction peaks are observed even when the Mn^{2+} content is increased up to 40 mol% (Fig. 1c and d). Nevertheless, extra $\text{NaMn}_3\text{F}_{10}$ peaks begin to appear when the Mn^{2+} content reaches 50 mol% (Fig. 1e). In contrast, diffraction peaks relevant to Fe_3O_4 are not observed in any of the XRD curves, perhaps because the NPs are composed of smaller Fe_3O_4 NPs coated by a higher percentage of $\text{NaYF}_4:\text{Yb/Tm}$ layer.⁴⁷ These findings reveal that Mn^{2+} doping can also promote the hexagonal to cubic phase transformation in the presence of Fe_3O_4 NPs.

To further reveal the phase and size control, $\text{Fe}_3\text{O}_4@ \text{Mn}^{2+}$ -doped $\text{NaYF}_4:\text{Yb/Tm}$ NPs (doped with different amounts of Mn^{2+}) were characterized by TEM (Fig. 2). The TEM images show that the sample prepared without Mn^{2+} doping is composed of hexagonal micro rods (β -phase) and small cubic NPs (α -phase) (Fig. 2a and b).⁴⁸ The addition of Mn^{2+} , as demonstrated in Fig. 2c–f, forms high-quality uniform OA- $\text{Fe}_3\text{O}_4@ \text{Mn}^{2+}$ -doped $\text{NaYF}_4:\text{Yb/Tm}$ NPs with the pure α -phase structure. The inset in Fig. 2e demonstrates the excellent dispersity of the OA coated $\text{Fe}_3\text{O}_4@ 40\% \text{Mn}^{2+}$ -doped $\text{NaYF}_4:\text{Yb/Tm}$ NPs, which could potentially exist as a magnetic fluid. Fig. 2g shows the typical selected area electron diffraction (SAED) pattern of the $\text{Fe}_3\text{O}_4@ \text{Mn}^{2+}$ -doped $\text{NaYF}_4:\text{Yb/Tm}$ NPs in Fig. 2e, in which the formation of the pure α -phase structure is evident.

Fig. 2g also shows a very clear diffraction ring corresponding to the α crystalline NaYF_4 (111), (200), (220), (311), (222), and (400) faces, which is consistent with the XRD results. A high-resolution TEM (HRTEM) image (Fig. 2h) of a single particle (shown in Fig. 2e) shows that the measured interplanar spacing of the Fe_3O_4 cores and Mn^{2+} -doped $\text{NaYF}_4:\text{Yb/Tm}$ shell are approximately 0.25 nm and 0.31 nm, respectively, which agree

well with the separation between the (311) lattice planes of the magnetite face-centered cubic structure and the (111) lattice planes of cubic NaYF_4 . Thus, the HRTEM image shown in Fig. 2h demonstrates successful connection between magnetic seed nanocrystals and the Mn^{2+} -doped $\text{NaYF}_4:\text{Yb/Tm}$ shell.

To reveal the impact of Mn^{2+} doping on the UCL properties, the UCL spectra of $\text{Fe}_3\text{O}_4@ \text{Mn}^{2+}$ -doped $\text{NaYF}_4:\text{Yb/Tm}$ NPs were studied. Fig. 3 shows the effect of various Mn^{2+} co-doping contents on the UCL of $\text{Fe}_3\text{O}_4@ \text{Mn}^{2+}$ -doped $\text{NaYF}_4:\text{Yb/Tm}$ NPs. Following the 980 nm laser excitation at room temperature, the UCNPs without Mn^{2+} doping exhibit an intense NIR emission (~ 800 nm) and a weak red emission (~ 690 nm). Tm^{3+} ions are used as activators to generate the emission from the NIR excitation. The Yb^{3+} emissions can be attributed to transition from the ground state energy level ($^2\text{F}_{7/2}$) to the excited state energy level ($^2\text{F}_{5/2}$) to Tm^{3+} . Tm^{3+} is excited from its ground state ($^3\text{H}_6$) to its excited state ($^3\text{H}_5$) by absorbing the transition. The NIR emission (~ 800 nm) originates from the ($^3\text{H}_4$) state to the ($^3\text{H}_6$) ground state. The NIR and red emissions are enhanced as the Mn^{2+} doping concentrations increase. The overall upconversion emissions reach a maximum value at 40 mol% Mn^{2+} . Nonradiative energy transfer of Tm^{3+} from the ($^1\text{D}_2$) and ($^1\text{G}_4$) states to the ($^4\text{T}_1$) state of the Mn^{2+} ions followed by a back energy transfer to the ($^3\text{F}_2$) state of Tm^{3+} enhances the fluorescence intensity and possibly improves the transition emission.⁴⁹ The decrease of the UCL intensity at high Mn^{2+} contents (50 mol%) could be caused by the exchange interaction between Mn^{2+} ions, which is depicted in Fig. 3, and significant distortion of the lattice, which induces concentration quenching, thus reducing the UCL intensity.^{50,51} The result reveals that Mn^{2+} doping is a general method to tune the crystal structure, size, and shape of UCNPs. According to the above result, the OA coated $\text{Fe}_3\text{O}_4@ 40\% \text{Mn}^{2+}$ -doped $\text{NaYF}_4:\text{Yb/Tm}$ NPs were chosen as the studying object in the following work.

3.2. Hydrophobic to hydrophilic transfer of $\text{Fe}_3\text{O}_4@ \text{Mn}^{2+}$ -doped $\text{NaYF}_4:\text{Yb/Tm}$ NPs

Here, an amphiphilic polymer ($\text{C}_{18}\text{PMH-mPEG}$) was synthesized by the reaction of C_{18}PMH with amine-functionalized methyl ether poly(ethylene glycol). The as-prepared hydrophobic $\text{Fe}_3\text{O}_4@ 40\% \text{Mn}^{2+}$ -doped $\text{NaYF}_4:\text{Yb/Tm}$ NPs were then transferred to a hydrophilic phase after coating them with $\text{C}_{18}\text{PMH-mPEG}$. The octadecene chains present in the alternating $\text{C}_{18}\text{PMH-mPEG}$ intercalate with the oleate ligands present on the surface of the $\text{Fe}_3\text{O}_4@ 40\% \text{Mn}^{2+}$ -doped $\text{NaYF}_4:\text{Yb/Tm}$ NPs because of hydrophobic interactions, while the anhydride rings and the mPEG segments in the polymer are exposed to the solvent. The efficacy of the $\text{C}_{18}\text{PMH-mPEG}$ coating is probed using several complementary techniques. Firstly, the ligand change was investigated using FTIR. For OA coated $\text{Fe}_3\text{O}_4@ 40\% \text{Mn}^{2+}$ -doped $\text{NaYF}_4:\text{Yb/Tm}$ NPs, the peaks at 2938 and 2868 cm^{-1} are assigned to the asymmetric and symmetric stretching vibrations of methylene ($-\text{CH}_2-$) in the long alkyl chain of OA, and the band at 1468 cm^{-1} is attributed to symmetric stretch vibrations of ($\text{RCOO}-$), indicating that OA is coated on the surface of the OA coated $\text{Fe}_3\text{O}_4@ 40\%$



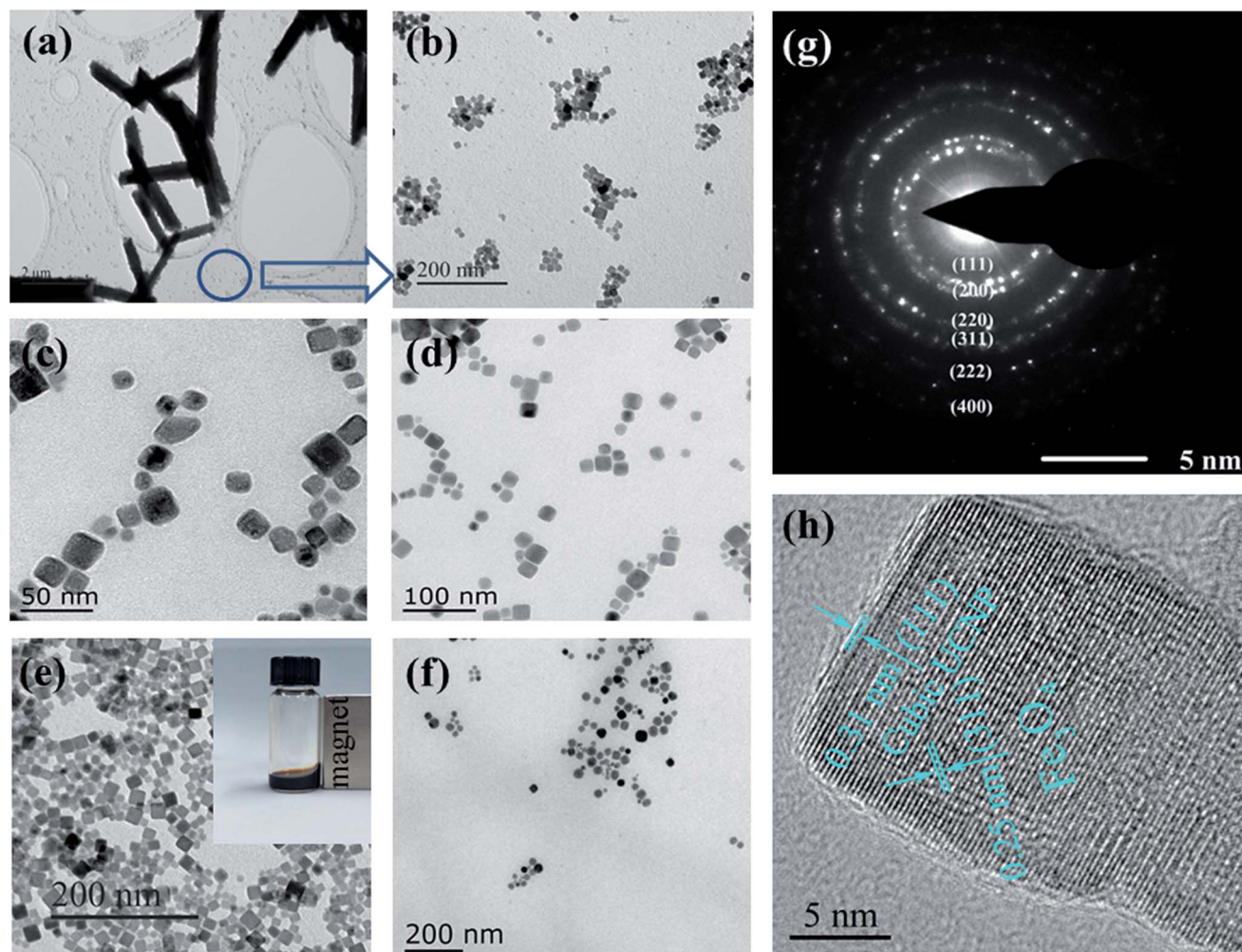


Fig. 2 (a–f) Typical TEM images of OA coated $\text{Fe}_3\text{O}_4@\text{NaYF}_4:\text{Yb/Tm}$ NPs doped with different amounts of Mn^{2+} (0, 20, 30, 40, and 50 mol%, respectively), (g) SAED of NPs in (e), and (h) HRTEM image of a single particle in (e). The inset of (e) shows a photographic image of the chloroform solution of OA coated $\text{Fe}_3\text{O}_4@40\% \text{Mn}^{2+}$ -doped $\text{NaYF}_4:\text{Yb/Tm}$ NPs under a magnet.

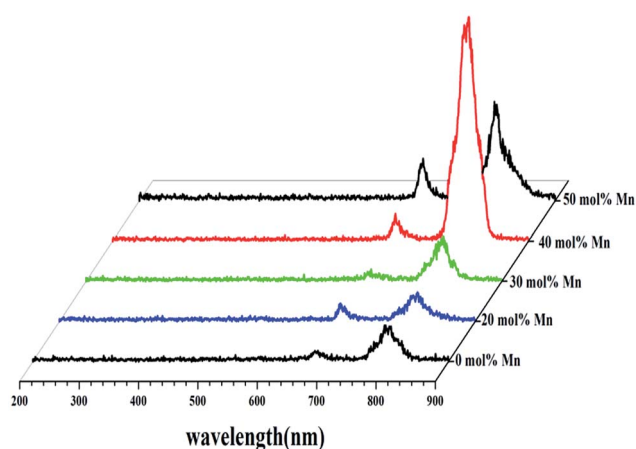


Fig. 3 UCL spectra of OA coated $\text{Fe}_3\text{O}_4@\text{NaYF}_4:\text{Yb/Tm}$ NPs co-doped with $\text{Mn}^{2+} = 0, 20, 30, 40$, and $50 \text{ mol}\%$ under the excitation of a 980 nm diode laser.

Mn^{2+} -doped $\text{NaYF}_4:\text{Yb/Tm}$ NPs (Fig. 4a). For the curve of $\text{C}_{18}\text{PMH-mPEG}$ coated $\text{Fe}_3\text{O}_4@40\% \text{Mn}^{2+}$ -doped $\text{NaYF}_4:\text{Yb/Tm}$ NPs, the new peak at 1116 cm^{-1} is attributed to $-\text{C}-\text{O}-$ in mPEG, and the new peak at 1662 cm^{-1} corresponds to the absorption of the carbonyl ($\text{C}=\text{O}$), which suggests the formation of a $\text{C}_{18}\text{PMH-mPEG}$ layer on the $\text{Fe}_3\text{O}_4@40\% \text{Mn}^{2+}$ -doped $\text{NaYF}_4:\text{Yb/Tm}$ NPs.

Fig. 5 shows TEM images of the $\text{Fe}_3\text{O}_4@40\% \text{Mn}^{2+}$ -doped $\text{NaYF}_4:\text{Yb/Tm}$ NPs before and after polymer coating. Compared with the OA coated $\text{Fe}_3\text{O}_4@40\% \text{Mn}^{2+}$ -doped $\text{NaYF}_4:\text{Yb/Tm}$ NPs (Fig. 5a), after modification with $\text{C}_{18}\text{PMH-mPEG}$ the $\text{Fe}_3\text{O}_4@40\% \text{Mn}^{2+}$ -doped $\text{NaYF}_4:\text{Yb/Tm}$ NPs maintain the cubic phase structure (show in Fig. 5b). In addition, the $\text{C}_{18}\text{PMH-mPEG}$ coated $\text{Fe}_3\text{O}_4@40\% \text{Mn}^{2+}$ -doped $\text{NaYF}_4:\text{Yb/Tm}$ NPs were separated from each other without observable aggregation, suggesting that they were effectively stabilized in aqueous solution (Fig. 5b).

Fig. 6 shows the magnetic hysteresis measurements of the prepared $\text{Fe}_3\text{O}_4@40\% \text{Mn}^{2+}$ -doped $\text{NaYF}_4:\text{Yb/Tm}$ NPs before and after polymer coating, measured at room temperature. The field-



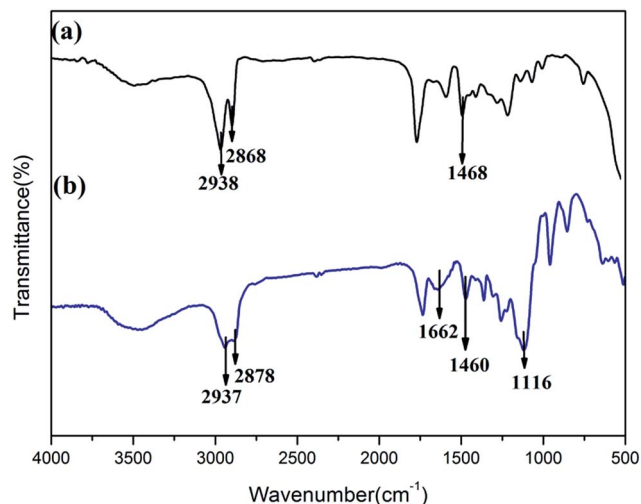


Fig. 4 FTIR spectra of OA (a) and C₁₈PMH-mPEG (b) coated Fe₃O₄@40% Mn²⁺-doped NaYF₄:Yb/Tm NPs.

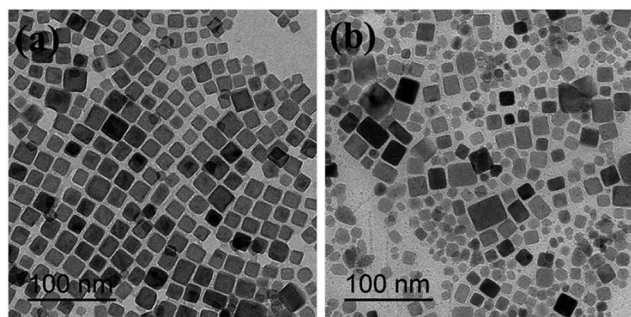


Fig. 5 TEM images of OA (a) and C₁₈PMH-mPEG (b) coated Fe₃O₄@40% Mn²⁺-doped NaYF₄:Yb/Tm NPs.

dependent magnetization plots illustrate that OA coated Fe₃O₄@40% Mn²⁺-doped NaYF₄:Yb/Tm NPs (see Fig. 6a) are superparamagnetic with saturation magnetization values of approximately 3.1 emu g⁻¹ at 25 °C. The C₁₈PMH-mPEG coated Fe₃O₄@40% Mn²⁺-doped NaYF₄:Yb/Tm NPs (see Fig. 6b) exhibit a saturation magnetization value of 2.4 emu g⁻¹, which is significantly lower than that of OA coated Fe₃O₄@40% Mn²⁺-doped NaYF₄:Yb/Tm NPs. This may be due to the C₁₈PMH-mPEG polymer coating on the Fe₃O₄@40% Mn²⁺-doped NaYF₄:Yb/Tm NPs.

Fig. 7 shows the UCL properties of the Fe₃O₄@40% Mn²⁺-doped NaYF₄:Yb/Tm NPs before and after polymer coating. The UCL intensity of the C₁₈PMH-mPEG coated Fe₃O₄@40% Mn²⁺-doped NaYF₄:Yb/Tm NPs is slightly reduced compared to the original hydrophobic NPs. This can be attributed to the nonradiative decay of the electronically excited states of the dopant lanthanide ions caused by surface ligands and water molecules.^{40,41} Even so, the C₁₈PMH-mPEG coated Fe₃O₄@40% Mn²⁺-doped NaYF₄:Yb/Tm NPs still exhibit good fluorescence properties. The inset in the top left corner shows that complete transfer of the Fe₃O₄@40% Mn²⁺-doped NaYF₄:Yb/Tm NPs from the bottom chloroform layer to the top water layer is achieved,

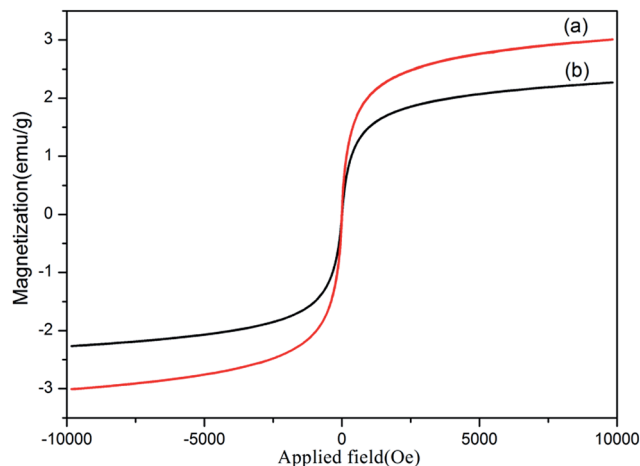


Fig. 6 Room-temperature magnetic hysteresis loop for OA (a) and C₁₈PMH-mPEG (b) coated Fe₃O₄@40% Mn²⁺-doped NaYF₄:Yb/Tm NPs.

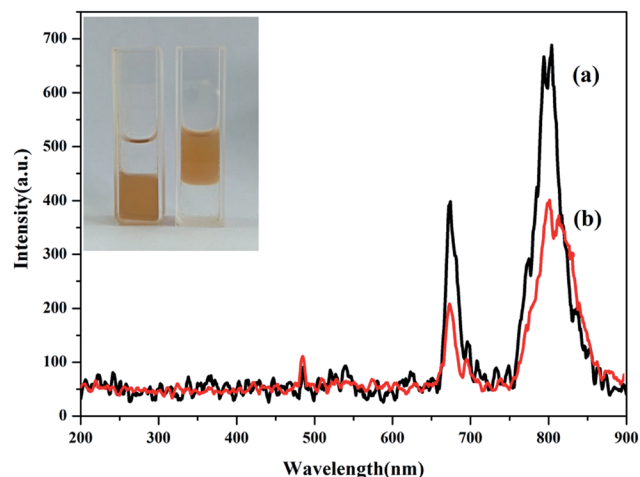


Fig. 7 Upconversion emission spectra of (a) the chloroform solution of OA coated Fe₃O₄@40% Mn²⁺-doped NaYF₄:Yb/Tm NPs and (b) the water solution of C₁₈PMH-mPEG coated Fe₃O₄@40% Mn²⁺-doped NaYF₄:Yb/Tm NPs under 980 nm excitation. The insets show photographic images of Fe₃O₄@40% Mn²⁺-doped NaYF₄:Yb/Tm NPs dispersed in chloroform and water.

indicating that Fe₃O₄@40% Mn²⁺-doped NaYF₄:Yb/Tm NPs are successfully coated by C₁₈PMH-mPEG.

3.3. Cytotoxicity test

The cytotoxicity of the C₁₈PMH-mPEG coated Fe₃O₄@40% Mn²⁺-doped NaYF₄:Yb/Tm NPs was determined using HeLa cells and a standard Cell Counting Kit-8 (CCK-8) colorimetric assay. After 24 h of incubation with concentrations varying from 0.0625 to 1 mg mL⁻¹, the C₁₈PMH-mPEG coated Fe₃O₄@40% Mn²⁺-doped NaYF₄:Yb/Tm NPs exhibit a satisfactory biocompatibility (see Fig. 8). The cell viability is greater than 78%, even at a high-dose concentration of 1 mg mL⁻¹. These results indicate that these C₁₈PMH-mPEG coated Fe₃O₄@40% Mn²⁺-



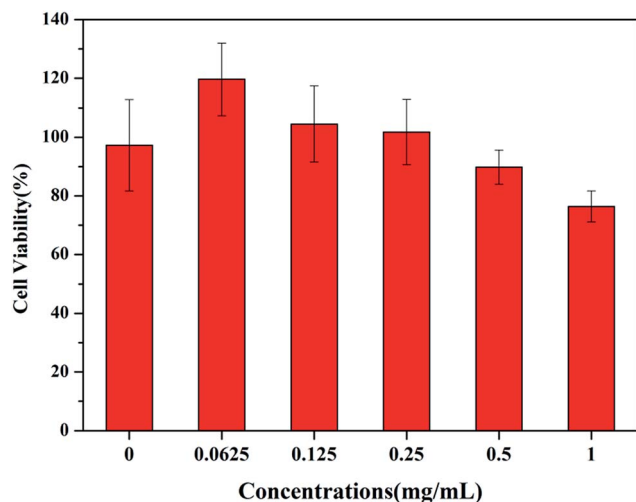


Fig. 8 *In vitro* cytotoxicity of C_{18} PMH-mPEG coated $Fe_3O_4@40\%$ Mn^{2+} -doped $NaYF_4:Yb/Tm$ NPs against HeLa cells at different concentrations after a 24 h incubation.

doped $NaYF_4:Yb/Tm$ NPs are potentially suitable for biomedical applications.

3.4. *In vivo* UCL imaging

To evaluate the NIR-to-NIR UCL imaging ability of these C_{18} PMH-mPEG coated $Fe_3O_4@40\%$ Mn^{2+} -doped $NaYF_4:Yb/Tm$ NPs, a 5 week-old nude mouse (male) was anaesthetized and injected with $100\ \mu L$ of $0.8\ mg\ mL^{-1}$ C_{18} PMH-mPEG coated $Fe_3O_4@40\%$ Mn^{2+} -doped $NaYF_4:Yb/Tm$ NPs in the abdomen region for *in vivo* imaging. The injection depth was about 10 mm (estimated from the needle penetration). As shown in Fig. 9, the UCL imaging could be obtained from the injected sites using an EMCCD camera by collecting NIR emission signal at $800 \pm 12\ nm$. In particular, region of interest (ROI) analysis of the UCL signal ($\lambda_{em} = 800 \pm 12\ nm$) reveals a high signal-to-noise ratio (~ 26) between the abdomen region and the background. The high contrast UCL image with ultra-low auto-fluorescence interferences can be attribute to the antistokes luminescence feature of UCL as well as the wavelength of the emission light that falls within the NIR window for bioimaging ($700\text{--}1000\ nm$).⁴

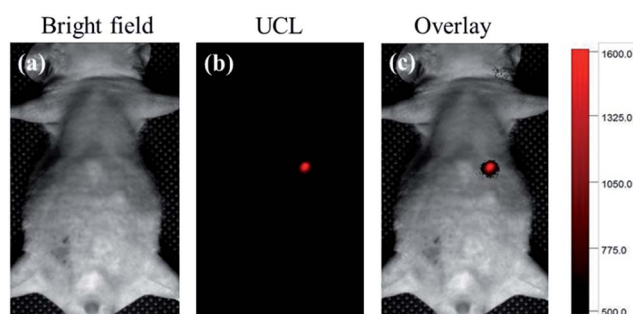


Fig. 9 *In vivo* UCL imaging. (a) Bright field image; (b) UCL image after injection with $100\ \mu L$ of C_{18} PMH-mPEG coated $Fe_3O_4@40\%$ Mn^{2+} -doped $NaYF_4:Yb/Tm$ NPs ($0.8\ mg\ mL^{-1}$) in the abdomen (power density of $80\ mW\ cm^{-2}$, $\lambda_{excitation} = 980\ nm$, $\lambda_{emission} = 800 \pm 12\ nm$); (c) merged image of bright field image and the UCL signals.

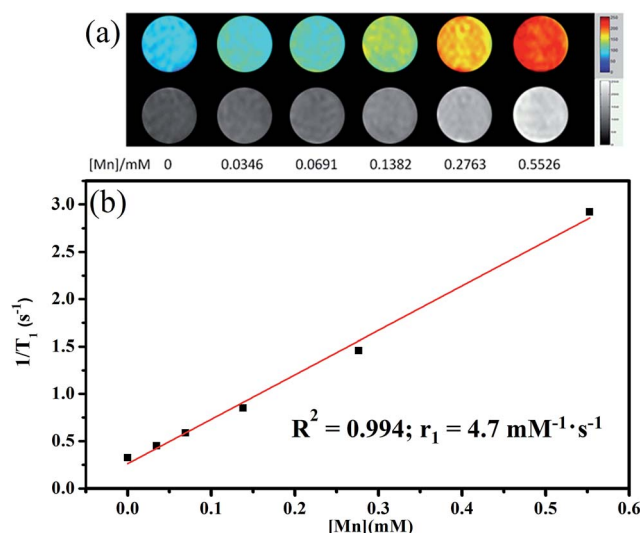


Fig. 10 Color T_1 -weighted images (a) and linear fitting of $1/T_1$ (b) of the C_{18} PMH-mPEG coated $Fe_3O_4@40\%$ Mn^{2+} -doped $NaYF_4:Yb/Tm$ NPs with different Mn concentrations. The color bar from blue to red indicates the gradual increase of the MR signal intensity.

3.5. T_1/T_2 -weighted MRI

The elemental composition of the C_{18} PMH-mPEG coated $Fe_3O_4@40\%$ Mn^{2+} -doped $NaYF_4:Yb/Tm$ NPs was further analyzed by ICP-MS, where the Fe/Mn molar ratio was estimated to be 3.54 : 1. To explore the T_1 -weighted imaging performance, MR phantom studies of the C_{18} PMH-mPEG coated $Fe_3O_4@40\%$ Mn^{2+} -doped $NaYF_4:Yb/Tm$ NPs dispersed in water at different Mn^{2+} concentrations were investigated (Fig. 10). As shown in Fig. 10a, the brighter signals in the T_1 -weighted images increase

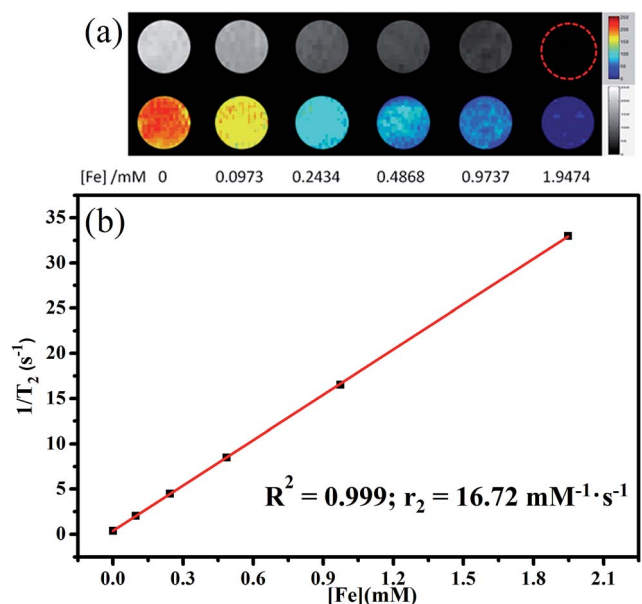


Fig. 11 Color T_2 -weighted images (a) and linear fitting of $1/T_2$ (b) of the C_{18} PMH-mPEG coated $Fe_3O_4@40\%$ Mn^{2+} -doped $NaYF_4:Yb/Tm$ NPs with different Fe concentrations. The color bar from blue to red indicates the gradual increase of the MR signal intensity.



as a function of the Mn^{2+} concentration (0–0.5526 mM). The T_1 relaxivity coefficient (r_1) for the C_{18}PMH -mPEG coated Fe_3O_4 @40% Mn^{2+} -doped $\text{NaYF}_4\text{:Yb/Tm}$ NPs could also be calculated from the curve of $1/T_1$ versus the Mn^{2+} concentration (Fig. 10b). The data show that r_1 is $4.7 \text{ mM}^{-1} \text{ s}^{-1}$ which is close to the relaxivity of commercial Gd-diethylenetriaminepentaacetic acid ($4.82 \text{ mM}^{-1} \text{ s}^{-1}$).

To demonstrate the potential to use the NPs for T_2 -weighted MRI, MR phantom studies of the NPs as a function of Fe concentration were also performed (Fig. 11). T_2 -weighted MR images (Fig. 11a) reveal that the brightness decreases with increasing Fe concentrations (0–1.9474 mM). Meanwhile, the T_2 relaxation rate ($1/T_2$) increases linearly with respect to the Fe concentration, and the slope (r_2 relaxivity) is calculated to be $16.72 \text{ mM}^{-1} \text{ s}^{-1}$ (Fig. 11b). Although, the r_2 relaxivity of the C_{18}PMH -mPEG coated Fe_3O_4 @40% Mn^{2+} -doped $\text{NaYF}_4\text{:Yb/Tm}$ NPs is lower than that of many MRI contrasts, the content of Fe_3O_4 here could be tuned to increase the r_2 relaxivity.

4. Conclusions

In summary, we synthesized core@shell OA-coated Fe_3O_4 @ Mn^{2+} -doped $\text{NaYF}_4\text{:Yb/Tm}$ NPs using a hydrothermal method. Besides the enhancement of the NIR UCL (UCL band at $\sim 800 \text{ nm}$), the control of the phase and size of these NPs was achieved by Mn^{2+} doping. Furthermore, the water-dispersible Fe_3O_4 @40% Mn^{2+} -doped $\text{NaYF}_4\text{:Yb/Tm}$ NPs were obtained by coating with an amphiphilic polymer (C_{18}PMH -mPEG), which exhibited good biocompatibility. Moreover, the prepared C_{18}PMH -mPEG coated Fe_3O_4 @40% Mn^{2+} -doped $\text{NaYF}_4\text{:Yb/Tm}$ NPs could be used for *in vivo* NIR to NIR imaging. The developed NPs could also be used as dual-mode T_1/T_2 -weighted MRI because of the co-existence of Fe_3O_4 and Mn^{2+} in the NPs. We expect that such multifunctional NPs that combine the advantages of magnetic drug delivery, NIR-to-NIR UCL, and MRI contrast, will find applications in anticancer therapy.

Acknowledgements

This work was supported by the National Natural Science Foundation of China (51273220), the Fundamental Research Funds for the Central Universities (2017NZZYQN17). The authors thank Prof. Fuyou Li, Prof. Wei Feng and Cong Cao from FuDan University, who gave many instructions on UCL imaging.

References

- 1 B. R. Smith and S. S. Gambhir, *Chem. Rev.*, 2017, **117**, 901.
- 2 O. S. Wolfbeis, *Chem. Soc. Rev.*, 2015, **44**, 4743.
- 3 A. Xia, Y. Gao, J. Zhou, C. Y. Li, T. S. Yang, D. M. Wu, L. M. Wu and F. Y. Li, *Biomaterials*, 2011, **32**, 7200.
- 4 B. Shen, Y. L. Gao, Q. Y. Liu, S. M. Cheng, W. Feng and F. Y. Li, *RSC Adv.*, 2017, **7**, 21625.
- 5 X. Wang, M. Tu, K. Yan, P. Li, L. Pang, Y. Gong, Q. Li, R. Liu, Z. Xu, H. Xu and P. K. Chu, *ACS Appl. Mater. Interfaces*, 2015, **7**, 24523.
- 6 L. Cheng, K. Yang, Y. Li, J. Chen, C. Wang, M. Shao, S. T. Lee and Z. Liu, *Angew. Chem., Int. Ed.*, 2011, 7385.
- 7 L. Zhang, Y. S. Wang, Y. Yang, F. Zhang, W. F. Dong, S. Y. Zhou, W. H. Pei, H. D. Chen and H. B. Sun, *Chem. Commun.*, 2012, **48**, 11238.
- 8 Z. L. Qin, S. N. Du, Y. Luo, Z. J. Liao, F. Zuo, J. B. Luo and D. Liu, *Appl. Surf. Sci.*, 2016, **378**, 174.
- 9 X. J. Zhu, W. Feng, J. Chang, Y. W. Tan, J. C. Li, M. Chen, Y. Sun and F. Y. Li, *Nat. Commun.*, 2016, **7**, 10437.
- 10 L. Zhou, R. Wang, C. Yao, X. Li, C. Wang, X. Zhang, C. Xu, A. Zeng, D. Zhao and F. Zhang, *Nat. Commun.*, 2015, **6**, 6938.
- 11 N. M. Idris, M. K. Gnanasammandhan, J. Zhang, P. C. Ho, R. Mahendran and Y. Zhang, *Nat. Med.*, 2012, **18**, 1580.
- 12 J. Tang, L. Chen, J. Li, Z. Wang, J. Zhang, L. Zhang, Y. Luo and X. Wang, *Nanoscale*, 2015, **7**, 14752.
- 13 Q. Liu, W. Feng, T. Yang, T. Yi and F. Li, *Nat. Protoc.*, 2013, **8**, 2033.
- 14 B. Shen, Y. L. Gao, Q. Y. Liu, S. M. Cheng, W. Feng and F. Y. Li, *RSC Adv.*, 2017, **7**, 21625.
- 15 N. N. Dong, M. Pedroni, F. Piccinelli, G. Conti, A. Sbarbati, J. E. Ramírez Hernández, L. M. Maestro, M. C. I. Cruz, F. SanzRodríguez, A. Juarranz, F. Chen, F. Vetrone, J. A. Capobianco, J. G. S. MarcoBettinelli, D. Jaque and A. Speghini, *ACS Nano*, 2011, **5**, 8665.
- 16 M. Nyk, R. Kumar, T. Y. Ohulchanskyy, E. J. Bergey and P. N. Prasad, *Nano Lett.*, 2008, **8**, 3834.
- 17 M. Hu, D. D. Ma, Y. Z. Cheng, C. C. Liu, Z. P. Zhang, Y. J. Cai, S. Wu and R. F. Wang, *J. Mater. Chem. B*, 2017, **5**, 2662.
- 18 Y. T. Zhang, Y. L. Shen, M. Liu, Y. Han, X. L. Mo, R. B. Jiang, Z. B. Lei, Z. H. Liu, F. Shi and W. P. Qin, *CrystEngComm*, 2017, **19**, 1304.
- 19 D. Yin, C. Wang, J. Ouyang, K. Song, B. Liu, X. Cao, L. Zhang, Y. Han, X. Long and M. Wu, *Dalton Trans.*, 2014, **43**, 12037.
- 20 J. Wang, F. Wang, C. Wang, Z. Liu and X. G. Liu, *Angew. Chem., Int. Ed.*, 2011, **50**, 10369.
- 21 G. Tian, Z. J. Gu, L. J. Zhou, W. Y. Yin, X. X. Liu, L. Yan, S. Jin, W. L. Ren, G. M. Xing, S. J. Li and Y. L. Zhao, *Adv. Mater.*, 2012, **24**, 1226.
- 22 S. J. Zeng, Z. G. Yi, W. Lu, C. Qian, H. B. Wang, L. Rao, T. M. Zeng, H. R. Liu, H. J. Liu, B. Fei and J. H. Hao, *Adv. Funct. Mater.*, 2014, **24**, 4051.
- 23 C. Wang, L. Cheng, Y. M. Liu, X. J. Wang, X. X. Ma, Z. Y. Deng, Y. G. Li and Z. Liu, *Adv. Funct. Mater.*, 2013, **23**, 3077.
- 24 X. Y. Li, X. W. Liu, D. M. Chevrier, X. Qin, X. J. Xie, S. Y. Song, H. J. Zhang, P. Zhang and X. G. Liu, *Angew. Chem.*, 2015, **127**, 13510.
- 25 G. Tian, W. Ren, L. Yan, S. Jian, Z. J. Gu, L. Zhou, S. Jin, W. Yin, S. Li and Y. Zhao, *Small*, 2013, **9**, 1929.
- 26 Y. B. Li, X. L. Li, Z. L. Xue, M. M. Jiang, S. J. Zeng and J. H. Hao, *Adv. Healthcare Mater.*, 2017, **6**, 1601231.
- 27 Z. Y. Huang, H. P. Gao and Y. L. Mao, *RSC Adv.*, 2016, **6**, 83321.
- 28 J. Zhou, Z. G. Lu, G. G. Shan, S. H. Wang and Y. Liao, *Biomaterials*, 2014, **35**, 368.
- 29 E. Shah, P. Upadhyay, M. Singh, M. S. Mansuri, R. Begum, N. Sheth and H. P. Soni, *New J. Chem.*, 2016, **40**, 9507.



- 30 N. D. Thorat, R. A. Bohara, H. M. Yadav and S. A. M. Tofail, *RSC Adv.*, 2016, **6**, 94967.
- 31 Y. Chen, H. Chen, S. Zhang, F. Chen, S. Sun and Q. He, *Biomaterials*, 2012, **33**, 2388.
- 32 H. Yang, Y. Zhuang, H. Hu, X. Du, C. Zhang and X. Shi, *Adv. Funct. Mater.*, 2010, **20**, 1733.
- 33 L. Cheng, K. Yang, Y. G. Li, J. H. Chen, C. Wang and M. W. Shao, *Angew. Chem., Int. Ed.*, 2011, **50**, 7385.
- 34 H. Yang, C. Zhang, X. Shi, H. Hu, X. Du and Y. Fang, *Biomaterials*, 2010, **31**, 3667.
- 35 J. W. M. Bulte and D. L. Kraitichman, *NMR Biomed.*, 2004, **17**, 484.
- 36 L. Turyanska, F. Moro, A. Patané, J. Barr, W. Köckenberger, A. Taylor, H. M. Faas, M. Fowler, P. Wigmore, R. C. Trueman, H. E. L. Williams and N. R. Thomas, *J. Mater. Chem. B*, 2016, **4**, 6797.
- 37 J. C. Li, Y. Hu, W. J. Sun, Y. Luo, X. Y. Shi and M. W. Shen, *RSC Adv.*, 2016, **6**, 35295.
- 38 Z. J. Zhou, L. R. Wang, X. Q. Chi, J. F. Bao, L. J. Yang, W. X. Zhao, Z. Chen, X. M. Wang, X. Y. Chen and J. H. Gao, *ACS Nano*, 2013, **7**, 3287.
- 39 M. Borges, S. Yu, A. Laromaine, A. Roig, S. Suárez-García, J. Lorenzo, D. Ruiz-Molina and F. Novio, *RSC Adv.*, 2015, **5**, 86779.
- 40 O. Plohl, S. Kralj, B. Majaron, E. Fröhlich, M. Ponikvar-Svet, D. Makovec and D. Lisjak, *Dalton Trans.*, 2017, **46**, 6975.
- 41 R. Arppe, I. Hyppanen, N. Perala, R. Peltomaa, M. Kaiser, C. Wurth, S. Christ, U. Resch-Genger, M. Schaferling and T. Soukka, *Nanoscale*, 2015, **7**, 11746.
- 42 G. Prencipe, S. M. Tabakman, K. Welsher, Z. Liu, A. P. Goodwin, L. Zhang, J. Henry and H. J. Dai, *J. Am. Chem. Soc.*, 2009, **9**, 4787.
- 43 R. Y. Wei, Z. W. Wei, L. N. Sun, J. Z. Zhang, J. L. Liu, X. Q. Ge and L. Y. Shi, *ACS Appl. Mater. Interfaces*, 2016, **8**, 400.
- 44 P. An, F. Zuo, Y. P. Wu, J. H. Zhang, Z. H. Zheng, X. B. Ding and Y. X. Peng, *Chin. Chem. Lett.*, 2012, **23**, 1099.
- 45 Q. Ju, D. T. Tu, Y. S. Liu, R. F. Li, H. M. Zhu, J. C. Chen, Z. Chen, M. D. Huang and X. Y. Chen, *J. Am. Chem. Soc.*, 2012, **134**, 1323.
- 46 D. D. Yin, C. C. Wang, J. Ouyang, K. L. Song, B. Liu, X. Z. Cao, L. Zhang, Y. L. Han, X. Long and M. H. Wu, *Dalton Trans.*, 2014, **43**, 12037.
- 47 C. C. Mi, J. P. Zhang, H. Y. Gao, X. L. Wu, M. Wang, Y. F. Wu, Y. Q. Di, Z. R. Xu, C. B. Mao and S. K. Xu, *Nanoscale*, 2010, **2**, 1141.
- 48 X. Wang, Y. Bu and Y. Xiao, *J. Mater. Chem. C*, 2013, **1**, 3158.
- 49 S. Z. Wang, J. G. Zhang, H. Q. Chen and L. Wang, *J. Lumin.*, 2015, **168**, 82.
- 50 P. Ramasamy, P. Chandra, S. W. Rhee and J. Kim, *Nanoscale*, 2013, **5**, 8711.
- 51 J. Tang, L. Chen, J. Li, Z. Wang, J. H. Zhang, L. G. Zhang, Y. S. Luo and X. J. Wang, *Nanoscale*, 2015, **7**, 14752.

